POLITECNICO DI TORINO
Repository ISTITUZIONALE

Physical properties and tensile strength evolution of gypsum materials under different water content conditions

Original
Physical properties and tensile strength evolution of gypsum materials under different water content conditions / Wang, C., Wei, S., Zhang, D., Yang, Y., Yu, B., Pan, Y.. - In: CONSTRUCTION AND BUILDING MATERIALS. - ISSN 0950-0618. - 364:(2023). [10.1016/j.conbuildmat.2022.129865]

Availability:
This version is available at: 11583/2997252 since: 2025-02-06T14:17:27Z

Publisher:
Elsevier Ltd

Published
DOI:10.1016/j.conbuildmat.2022.129865

Terms of use:

This article is made available under terms and conditions as specified in the corresponding bibliographic description in the repository

Publisher copyright
Elsevier postprint/Author's Accepted Manuscript

© 2023. This manuscript version is made available under the CC-BY-NC-ND 4.0 license
http://creativecommons.org/licenses/by-nc-nd/4.0/.The final authenticated version is available online at:
http://dx.doi.org/10.1016/j.conbuildmat.2022.129865

(Article begins on next page)

28 November 2026

Physical properties and tensile strength evolution of gypsum materials under different water content conditions

Chongyang Wang [12], Sijiang Wei [3], Dongming Zhang [12*], Yushun Yang [4], Beichen Yu [12], Yisha Pan [5]

1. State Key Laboratory of Coal Mine Disaster Dynamics and Control, Chongqing University, Chongqing 400030, China.

2. School of Resources and Safety Engineering, Chongqing University, Chongqing 400030, China.

3. School of Energy Science and Engineering, Henan Polytechnic University, Jiaozuo 454000, Henan, China.

4. Faculty of Architecture and Civil Engineering, Huaiyin Institute of Technology, Huai'an 223001, Jiangsu, China

5. School of Surveying, Mapping and Land Information Engineering, Henan Polytechnic University, Jiaozuo 454000, Henan, China.

* Correspondence: zhangdm@cqu.edu.cn.

Abstract: To investigate the physical properties and tensile strength evolution of gypsum materials under different water content conditions, three groups of gypsum standard samples were prepared, including natural, saturated and dehydrated gypsum samples. Electron microscopy, composition analysis, Brazilian splitting tests and numerical simulation analysis were carried out. The results are as follows. The larger the water content of the samples is, the higher the content of $CaSO_4 \cdot 2H_2O$, the more flocculation structures on the surface, and the higher the longitudinal wave propagation speed. Saturation and dehydration change the composition of the sample and cause a change in its tensile strength and failure mode. The fitting effect of the modified Hoek–Brown criterion is obviously better than that of the modified Mohr–Coulomb criterion because it considers the influence of uniaxial compressive strength. The Balmer criterion introduces the index b and greatly improves its regression accuracy. The vertical compressive stress exhibits a concentrated distribution. At x=0, the peak value of the vertical load appears at the two ends of contact between the specimen and the indenter and gradually decreases from both ends to the centre. The horizontal stress is mainly tensile stress, and the value at x=0 is the theoretical tensile strength. It is uniformly distributed on the line directly affected by the vertical load and decreases to both ends of the specimen along the line. It is reduced to 0 at the left and right ends. The horizontal deformation arises from both sides of the disk tip and then spreads downwards in an arc during loading. The horizontal strain in the upper part of the disk is always larger than that in the lower part. The upper part reaches its tensile strength and then fails due to the continuous loading.

Keywords: gypsum, tensile strength, strength criterion, stress distribution, numerical simulation.

1. Introduction

In the field of architecture and geotechnical engineering, the tensile strength of brittle materials is the main parameter affecting the failure of engineering structures. As the main method of measuring the tensile strength of materials, the Brazilian splitting test has been widely used in construction, civil engineering, geotechnical engineering and other fields [1-6]. Saksala et al. conducted dynamic Brazilian disc tests on Kuru granite based on viscoplastic and damage mechanics constitutive models and finite element numerical techniques. The results show that the loading rate is linearly correlated with the indirect tensile strength of the Kulu granite disc [7]. Shen et al. investigated the tensile properties of hardened fly ash high-strength concrete. The experimental results showed that its tensile Young's modulus at an early age increased with increasing uniaxial tensile strength [8]. Li et al. analysed the relationship between the tensile strength and fracture area of cement paste specimens through laboratory tests. The results show that the tensile strength is negatively correlated with the addition of SCM and the W/B ratio [9]. Verma et al. used AUSBIT's Brazilian disc test, successfully conducted on concrete and various rocks, to evaluate the effectiveness of AUSBIT in controlling local dynamics using acoustic emission and digital

image correlation techniques [10]. Lochan et al. studied the tensile strength of glass fibre-reinforced polymer (GFRP) reinforcing bars through laboratory tests and proposed the three-point flexure test as an alternative for direct tensile testing of GFRP bars. It has been proven that flexural testing can provide an easy and reliable method for obtaining the tensile strength of GFRP reinforcing bars [11]. Gaedicke et al. studied the effect of porosity variation on the relationship between tensile strength and compressive strength through laboratory tests on 16 kinds of mixed materials [12]. Mardoukhi et al. studied the dynamic tensile behaviour of two granitic rocks using the Brazilian disc test and split Hopkinson compression bar. High strain rate Brazilian plate tests were carried out at -30 °C, -50 °C and -70 °C on samples without cyclic thermal loading. The results show that rocks with different microstructures respond differently to cyclic thermal loads. Lowering the test temperature will lead to an increase in the tensile strength of the two rocks being studied [13, 14]. Zhao et al. carried out a Brazilian disk split test on MSC cubes and analysed the effects of the water-cement ratio and stone powder content on the tensile strength of MSC. Forecast models of the long-term tensile strength of MSC were proposed [15].

The above studies on the tensile properties of rock and other materials have achieved many meaningful results [16-21]. Liang et al. discussed several kinds of common random distribution functions used to realize the heterogeneity of elastic damage models and studied a probability model of random distribution function failure processes under loading [22]. Yang et al. conducted Brazilian splitting and acoustic emission tests on seven groups of samples with different inclination angles. The results show that the direction of bedding has an important influence on the splitting strength and the final failure mode of shale samples. With the increase in bedding angle, the splitting strength of shale samples decreases gradually [23]. Aggelis studied the different characteristics of the signals emitted by different fracturing stages through acoustic emission monitoring of several kinds of concrete during the experiment and proposed several AE indices, which could be used to classify cracks according to their modes [24]. Jiang et al. used statistical analysis and hypothesis testing to study the random distribution characteristics of the characteristic strength and deformation parameters of two kinds of basalt and pointed out that dispersion is an inherent property of basalt, and only a certain number of repeated tests can reliably evaluate its basic mechanical properties [25]. Du et al. carried out a failure process test under the splitting load of a Brazilian disc of shale with different bedding inclination angles. By using digital image correlation technology, they studied the initiation time, spatial location, propagation law and fracture mechanism of microfractures in carbonized shale with different bedding directions [26]. To study the influence of the interface direction of hard rock and soft rock on its failure form, Li et al. carried out a Brazilian splitting test with multiple groups of loading angles on composite samples containing rock-cement mortar and studied the failure mechanism of the interface using PFC^{2D} software [27]. Yang used PFC^{2D} software with a built-in single disk discrete element model of the Brazilian splitting test, studied the radius ratio and the influence of eccentricity on the disc deformation and strength characteristics, and concluded that the stiffness of a single disk and the maximum tensile strength decrease with increasing radius ratio and increase with increasing eccentricity [28].

Finally, there are many studies on the influence of water content on rock properties [29-32]. Vasarhelyi statistically analysed the simple compressive strength and shear Young's modulus of 35 British sandstones. The test results of these sandstones under wet and dry conditions were analysed, and the petrophysical parameters were obtained [33]. Zhou et al. carried out compression and tensile tests on sandstone samples with different water contents. From the laboratory tests, reductions in the compressive and tensile strengths of sandstone under static and dynamic states in different saturation processes were observed [34]. Erguler et al. determined the uniaxial compressive strength, tensile strength and elastic modulus of several rock samples with different water contents. The results show that the uniaxial compressive strength, elastic modulus and tensile strength decrease by 90%, 93% and 90%, respectively, with increasing moisture content [35]. Daraei used the uniaxial compressive strength test results of 67 samples from eight rock types under dry, natural and saturated conditions to illustrate in detail the effect of water content on critical and failure strains [36]. Tang et al. tested the tensile strength of compacted clayey soil with different water contents and dry densities, and the results showed that the tensile

strength of compacted clayey soil significantly depends on the water content [37].

Although the above scholars have performed much research on deformation, strength and failure characteristics through tensile tests and the influence of water content on the mechanical properties of rock, there are few studies on the mechanism of tensile strength evolution with the microstructure and composition of the material under different water content conditions. In addition, studies on the stress and strain distribution of the loading axial plane in the Brazilian splitting test are also insufficient. Different water-rich times cause different water contents in roofs supporting water-rich tunnels and then change their physical and mechanical properties [33]. Therefore, it is of great significance to study the evolution characteristics of the physical properties and tensile strength of roof rock mass under different water content conditions. However, natural rock joints and fissures exhibit with strong anisotropy. The homogeneity of gypsum-like rock is good after many procedures, such as stirring and vibration. To exclude irrelevant variables, based on previous studies [38-42], this paper selects high-strength gypsum powder to prepare gypsum rocks under different water content conditions and carries out wave velocity tests, electron microscopy scanning, composition analysis, Brazilian splitting and other tests. The physical properties and tensile strength evolution of gypsum samples under different moisture contents were analysed. Three improved strength criteria were used to evaluate the tensile strength of the specimens. On this basis, the plane stress and deformation distributions of the specimens were analysed to provide theoretical reference for the failure and instability mechanism of water-rich rock masses in underground engineering.

2. Materials and Methods

2.1 Sample Preparation

Grade α high-strength gypsum powder, produced by Sichuan Hongtai Biochemical Co., Ltd., Nanchong, China, was selected. Its main component is $CaSO_4 \cdot 0.5H_2O$. A block was prepared according to a ratio of water to paste of 3:10, and a standard sample was processed. The processed samples were divided into three groups: natural, water-saturated and dehydrated samples. The specific preparation and grouping process can be found in the literature [38, 40]. We will not repeat it here.

2.2 Testing device

2.2.1 Ultrasound testing device

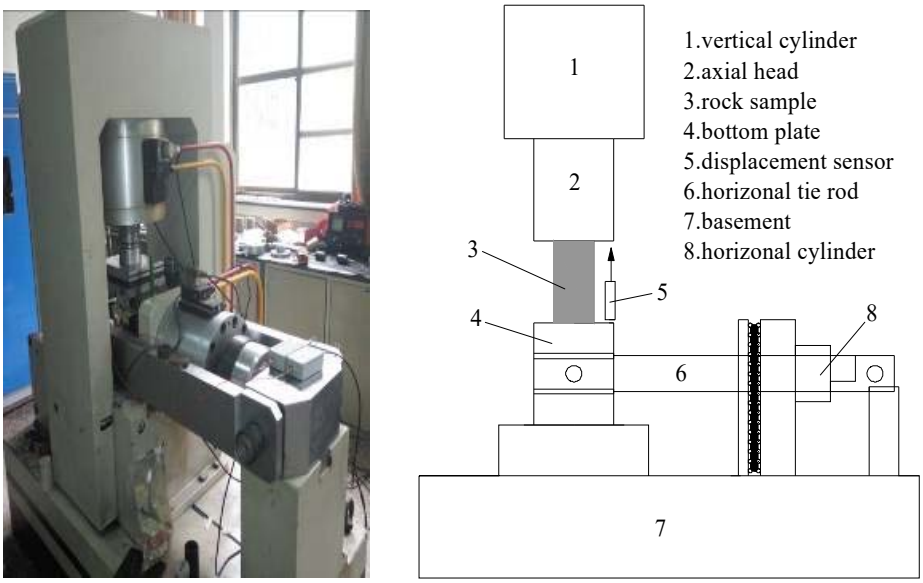
The samples were subjected to ultrasonic testing by using an UTA2001A ultrasonic inspection monitor, as shown in Figure 1. The UTA2001A system is an intelligent measuring instrument with a microprocessor. Its sampling frequency can be set to 10, 5, 2, and 1 MHz.



Figure 1. UTA2001A ultrasonic inspection monitor.

2.2.2 Mechanical testing device

The test was carried out on an RMT-150B electrohydraulic servo rock test system, as shown in Figure 2. The maximum axial load of the test system was 1000 kN. It can carry out tests such as rock uniaxial compression, indirect (direct) stretching and compression-shear tests.



(a) (b)

Figure 2. Electro-hydraulic servo rock test system of RMT-150B. (a) Test system. (b) Schematic diagram of uniaxial compression.

2.3 Test Methods

1) Longitudinal wave velocity measurement: The sampling frequency was 10 MHz. The samples were sealed in fresh bags in time before and after the test to avoid water absorption or dehydration of the samples in air (the same below).

2) Composition analysis of the samples: A D8-ADVANCE X-ray diffractometer was used to analyse the composition of the samples in each group to test the composition change characteristics of the samples under different water content conditions.

3) Microscopic composition analysis: The sample fragments with different water contents were analysed by a JSM-6390LV scanning electron microscopy (SEM) system.

4) Brazil splitting test: The test was carried out on an RMT-150B electrohydraulic servo test system. The test adopted the displacement control mode, and the loading rate was 0.005 mm/s.

3. Test results and analysis

3.1 Sample Characteristics

3.1.1 Physical Properties

The density, moisture content, wave velocity and other physical properties of the samples in different states were tested, as shown in Table 1 [38, 43].

In Table 1, the water content (f_w) is the relative value. In this paper, the water content of the samples in the high-temperature dehydration group is 0, and the water content of the natural group and the saturated group is calculated based on high-temperature dehydration group.

Table 1. Physical properties of the samples

Group	m (g)	f_w	ρ (g/cm^3)	v (m/s)
Natural	338.7	0.254	1.726	2967
Water-saturation	371.2	0.374	1.891	3017
Dehydration	270.2	0	1.377	1531

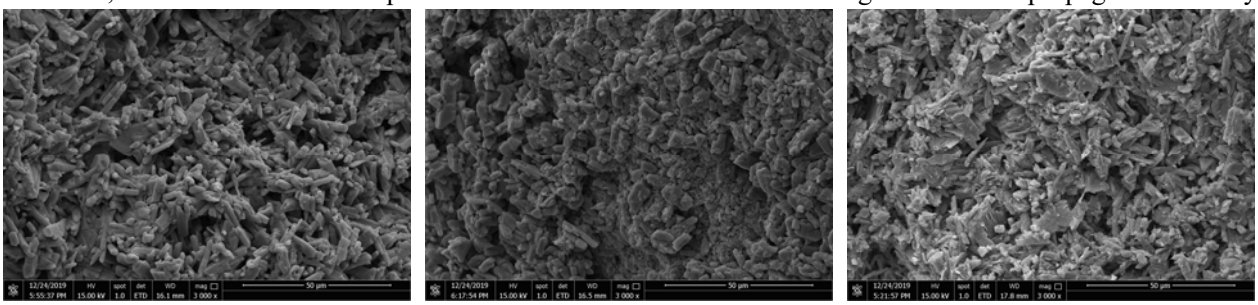
As seen in Table 1, the moisture content and longitudinal wave velocity of the samples in the saturated group are the largest, while those in the high-temperature dehydration group are the smallest. Due to the loss of crystal

water in the high-temperature environment, the internal structure of the samples was damaged, resulting in the samples in the high-temperature dehydration group having the lowest wave velocity. Compared with that of the natural group, the wave velocity of the high-temperature group was reduced by 48.4%. This may be due to the uneven heating of minerals inside the sample, resulting in uncoordinated deformation and expansion and then micromicroscopic cracks. At the same time, the cracking of crystallized water after heating causes corresponding physical and mechanical changes in the structure and material properties of the sample, resulting in a complex distribution of cracks and defects. When ultrasonic waves encounter cracks and defects in the propagation process, they must undergo refraction, diffraction and other phenomena. The weakening of the waveguide property and the increase in energy attenuation led to a decrease in the longitudinal wave velocity. The longitudinal wave velocity is closely related to the mechanical properties of samples after high-temperature dehydration.

3.1.2 Microscopic composition analysis

An FEI Quanta 250 FEG-SEM system was used to scan the microstructure of each sample used in this study. Figure 3 shows the scanning results with 3000× magnification [38, 39].

As seen from Figure 3, the interior of the remoulded sample under natural conditions is homogeneous and compact, with dense particles, smooth crystal fractures, sharp edges and corners, and partial lumps, as shown in Figure 3(a). The water-saturated sample contains more dihydrate gypsum, and the homogeneous compact edges and angles are not obvious in the sample, as shown in Figure 3(b). After dehydration at high temperature for 24 h, a large number of arranged and disordered prismatic crystals formed inside the sample, and microcracks were distributed among the crystals. Some crystals exhibited fracture phenomena, the fractures were clearly visible, and the number of micropores increased significantly, as shown in Figure 3(c). Combined with the physical properties presented in Section 3.1.1, the larger the moisture content of the sample is, the more flocculent structures on its surface and the higher the longitudinal wave propagation speed. The smaller the sample moisture content is, the more disordered the prisms on the surface and the lower the longitudinal wave propagation velocity.



(a) (b) (c)

Figure 3. Scanning results at 3000 times magnification. (a) Natural. (b) Water saturation. (c) Dehydration

3.1.3 Mineral composition analysis

Gypsum is a monoclinic crystalline mineral mainly composed of $CaSO_4 \cdot nH_2O$, which exists in various forms, such as $CaSO_4 \cdot H_2O$, $CaSO_4 \cdot 0.5H_2O$ and $CaSO_4 \cdot 2H_2O$, due to different water contents, as shown in Figure 4 [42]. There are great differences in the physical properties of gypsum materials with different water contents. Therefore, it is of great significance to explore the composition of samples under different water content conditions.

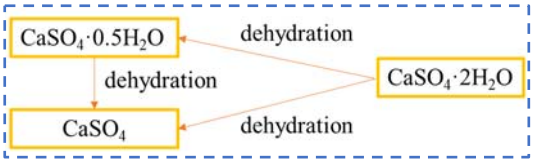
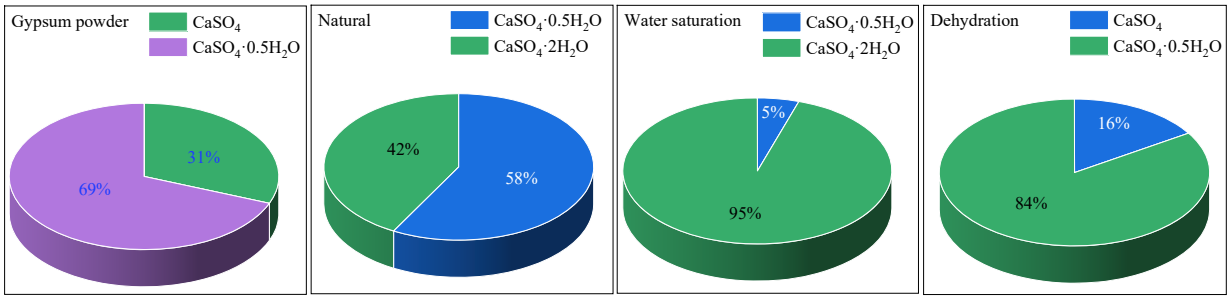


Figure 4. Schematic diagram of gypsum material composition changes under water absorption and dehydration.

X-ray diffraction tests were carried out on high-strength gypsum powder remoulded samples in different water cut states, and the main mineral crystal components were obtained, as shown in Figure 5.



(a) (b) (c) (d)

Figure 5. Main mineral components of gypsum powder remoulded samples. (a) Gypsum powder. (b) Natural. (c) Water saturation. (d) Dehydration.

As seen from Figure 5, after casting high-strength gypsum powder into the remoulded sample, calcium sulfate disappeared, mainly manifested as $CaSO_4$, the water content increased, and $CaSO_4·0.5H_2O$ became $CaSO_4·0.5H_2O$ and $CaSO_4·2H_2O$ by absorbing water. The main mineral composition of the saturated sample was the same as that of the natural sample, but the main difference is that the saturated sample contained a higher proportion of $CaSO_4·2H_2O$. After high-temperature dehydration at 220 °C, $CaSO_4·2H_2O$ became $CaSO_4$ and $CaSO_4·0.5H_2O$ by dehydration.

Combined with the analysis in Section 3.1.2, the flocculent structure on the surface of the water-saturated sample and natural sample is $CaSO_4·2H_2O$, while the rip-shaped crystal on the surface of the high-temperature dehydrated sample is $CaSO_4·0.5H_2O$. Through saturation and dehydration, different structural components are generated in the sample, and these structural components have a great influence on the physical properties (longitudinal wave velocity, microstructure, etc.) of the sample.

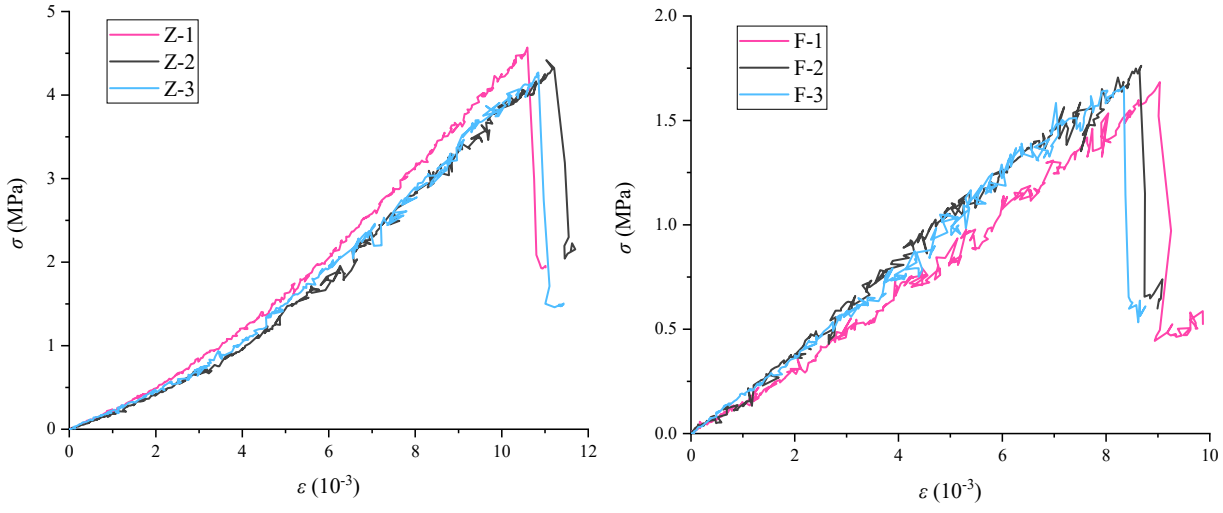
3.2 Stress–strain characteristics

The formula for calculating the tensile strength of each sample in different water content states is

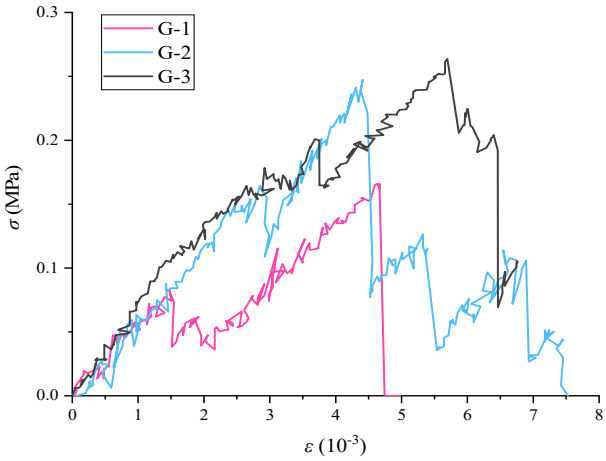
$$\sigma_t = \frac{2P}{\pi D t} \quad (1)$$

where σ_t is the tensile strength of rock, P is the failure load of the sample, D is the diameter of the sample, and t is the thickness of the sample.

According to Equation (1), the splitting tensile strength of each sample in different water cut states was calculated, and its stress–strain curve was drawn, as shown in Table 2 and Figure 6.



(a) (b)



(c)

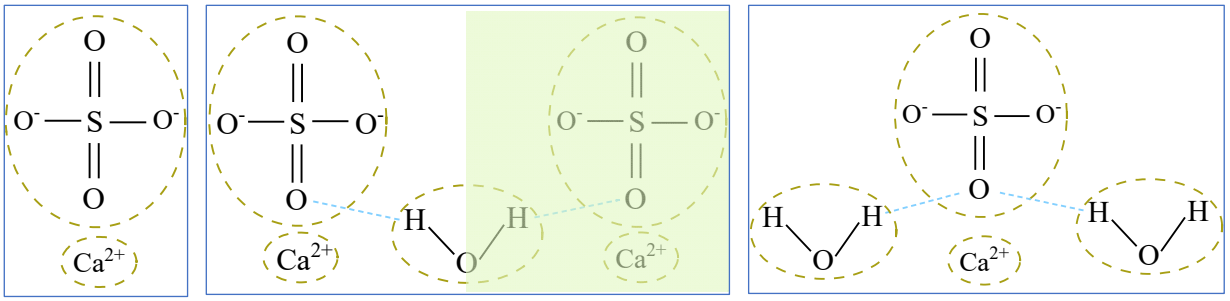
Figure 6. Stress-strain curves of each sample in Brazil splitting test. (a) Natural. (b) Water saturation. (c) Dehydration.

Meanwhile, by analysing the stress–strain curve of Figure 6, the tensile splitting failure process of natural, saturated and high-temperature dehydrated specimens can be divided into four stages: the compaction stage, elastic deformation stage, plastic deformation stage and failure stage. When the natural and saturated samples reached the peak tensile strength, the stress–strain curve dropped instantaneously, and the samples showed obvious brittle failure. However, the high-temperature dehydrated samples showed the characteristics of multiple splits during the splitting process, and the plastic deformation stage time became significantly longer. Moreover, when the load reached the peak value, the samples did not fail rapidly, showing certain plastic failure characteristics.

Table 2. Statistical table of tensile strength of gypsum rocks

Group	σ_t (MPa)	Group	σ_t (MPa)	Group	σ_t (MPa)
Natural	3.858	Water saturation	1.452	Dehydration	0.142
	3.939		1.53		0.264
	3.76		1.467		0.215
Mean value	3.85	Mean value	1.48	Mean value	0.207

This corresponds to the physical characteristics of the sample in Section 3.1. To further analyse the relationship between the strength and composition of the sample, the molecular structure diagram of the sample under different moisture content conditions is shown in Figure 7. The samples in the natural group contained more $CaSO_4 \cdot 0.5H_2O$. As Figure 7 (b) shows, $CaSO_4 \cdot 0.5H_2O$ belongs to the monoclinic system, and a $[SO_4]^{2-}$ tetrahedron and Ca^{2+} are connected into a layered structure parallel to the [1 0 0] and [0 1 0] surfaces. Half of the H_2O molecules are located in this channel and are connected with O^{2-} in $[SO_4]^{2-}$ by hydrogen bonds, making this a relatively stable state. This is the reason for the maximum tensile strength of the natural specimens.



(a) (b) (c)

Figure 7. Molecular structure of samples under different moisture content (a) $CaSO_4$. (b) $CaSO_4 \cdot 0.5H_2O$. (c) $CaSO_4 \cdot 2H_2O$

According to Figure 5(c), the composition of the water saturated sample is the same as that of the natural sample and includes $CaSO_4 \cdot 0.5H_2O$ and $CaSO_4 \cdot 2H_2O$. However, the content of $CaSO_4 \cdot 2H_2O$ in the water-saturated sample greatly increased. Figure 7 (c) shows that $CaSO_4 \cdot 2H_2O$ belongs to the monoclinic crystal system. A $[SO_4]^{2-}$ tetrahedron and Ca^{2+} are connected into a bilayer structure parallel to the [0 1 0] surface, and two H_2O molecules are distributed between the bilayer. Among them, the O^{2-} molecules in the $[SO_4]^{2-}$ tetrahedron and H_2O are connected by hydrogen bonds, demonstrating a relatively stable state. As a result, the tensile strength of the specimens in the water-saturated group was second only to that in the natural group, and the stress–strain curve characteristics of the specimens under Brazilian disc loading were similar to those in the natural group.

The dehydration group contained a large amount of $CaSO_4$. Figure 7 (a) shows that $CaSO_4$ belongs to the orthorhombic system, and the crystal structure is composed of $[SO_4]^{2-}$ tetrahedra and Ca^{2+}. Due to the loss of a large amount of free water and structural water in the oven, its physical and mechanical properties began to become extremely unstable, the tensile strength was greatly reduced, and it showed obvious plasticity during the loading process. This shows that high-temperature dehydration has an obvious deterioration effect on the sample.

3.3 Strength Characteristics

3.3.1 Mohr–Coulomb criterion

According to Mohr–Coulomb strength criterion [45],

$$\begin{cases} \tau = c + \sigma tan\varphi \\ \sigma_t = \dfrac{2c\ cos\varphi}{1 + sin\varphi} \end{cases} \tag{2}$$

where τ is the shear stress, σ is the normal stress, c is cohesion, and φ is the angle of internal friction.

Using Equation (2) to solve the tensile strength of the sample requires mechanical parameters such as cohesion and the internal friction angle. Based on previous laboratory tests, the basic mechanical parameters of the gypsum rocks used in this paper are summarized, as shown in Table 3 [39].

Table 3. Physical and mechanical properties of gypsum rocks

Group	c (MPa)	φ (°)	σ_c (MPa)
Natural	13.18	27	44.53
Water saturation	11.39	15	22.2
Dehydration	8.50	28.7	9.14

Substituting the mechanical parameter results in Table 3 into Equation (2), it can be rewritten as

$$\begin{cases} \tau_1 = 13.18 + 27\sigma_1 \\ \tau_2 = 11.39 + 15\sigma_2 \\ \tau_3 = 8.50 + 28.7\sigma_3 \end{cases} \tag{3}$$

Equation (3) can be used to preliminarily calculate the tensile strength σ_t of each sample under different water content conditions as follows:

$$\begin{cases} \sigma_{t1} = \dfrac{2 * 13.18 * cos27°}{1 + sin27°} = 16.1MPa \\ \sigma_{t2} = \dfrac{2 * 11.39 * cos15°}{1 + sin15°} = 17.5MPa \\ \sigma_{t3} = \dfrac{2 * 8.5 * cos28.7°}{1 + sin28.7°} = 10.1MPa \end{cases} \tag{4}$$

According to Equation (4), the tensile strength calculated by the Mohr–Coulomb criterion differs greatly from

the actual value, and the average value of the former is 8.6 times that of the latter. Therefore, it is necessary to propose a modified Mohr–Coulomb strength criterion:

$$\sigma_t' = \alpha \cdot \frac{2c\ cos\varphi}{1 + \theta sin\varphi} + \beta \tag{5}$$

In Equation (5), α, β and θ are the cohesion force correction coefficient, internal friction angle correction coefficient and intercept correction coefficient, respectively. Through the approximation of the formula and data, the value of each parameter can be calculated as follows:

$$\begin{cases} \alpha = 0.38 \\ \beta = -5.2 \\ \theta = 0.1 \end{cases} \tag{6}$$

By substituting Equation (6) into Equation (5), the modified value σ_t' of the tensile strength of each sample under different water content conditions is

$$\begin{cases} \sigma_{t1}' = 3.36MPa \\ \sigma_{t2}' = 2.97MPa \\ \sigma_{t3}' = 0.22MPa \end{cases} \tag{7}$$

To further compare the fitting degree of the modified Mohr–Coulomb strength with the experimental data, the tensile strength-water content curve was drawn, as shown in Figure 8.

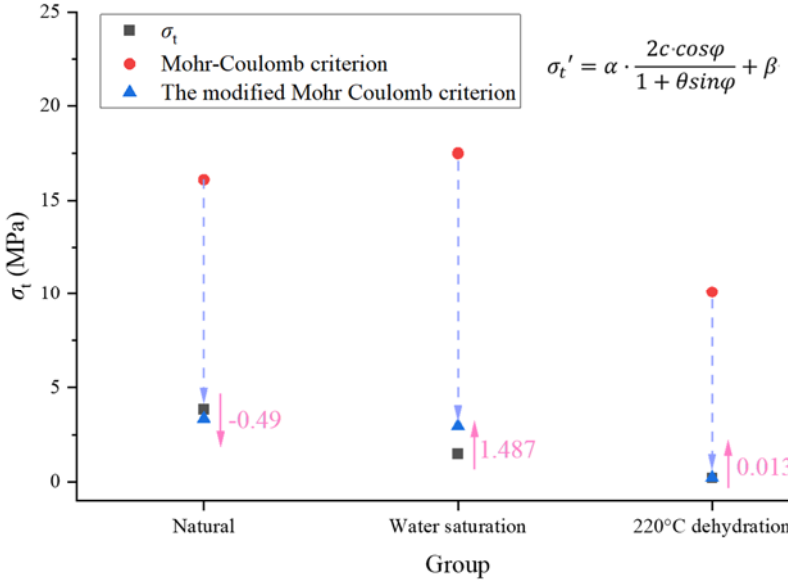


Figure 8. Tensile strength-water content curve under Mohr-Coulomb strength criterion.

As seen from Figure 8, the accuracy of the modified Mohr–Coulomb strength criterion is significantly improved compared with that before the modification. Compared with the original value, the average value of the modified Mohr–Coulomb strength criterion is 18% different, which can reflect the change law of the cohesion, internal friction angle and tensile strength of gypsum rock samples under different conditions to a certain extent.

3.3.2 Hoek–Brown criterion

According to the Hoek–Brown criterion [46, 47],

$$\sigma_1 = \sigma_3 + \sigma_c \sqrt{\frac{l\sigma_3}{\sigma_c} + 1}$$

where σ_1 and σ_3 are the maximum and minimum principal stresses at rock failure, respectively; l is the empirical parameter; and σ_c is the uniaxial compressive strength of rock.

According to Equation (8), the $\sigma_1 - \sigma_3$ curves of the triaxial test in the laboratory under the Hoek–Brown criterion are drawn, as shown in Figure 9.

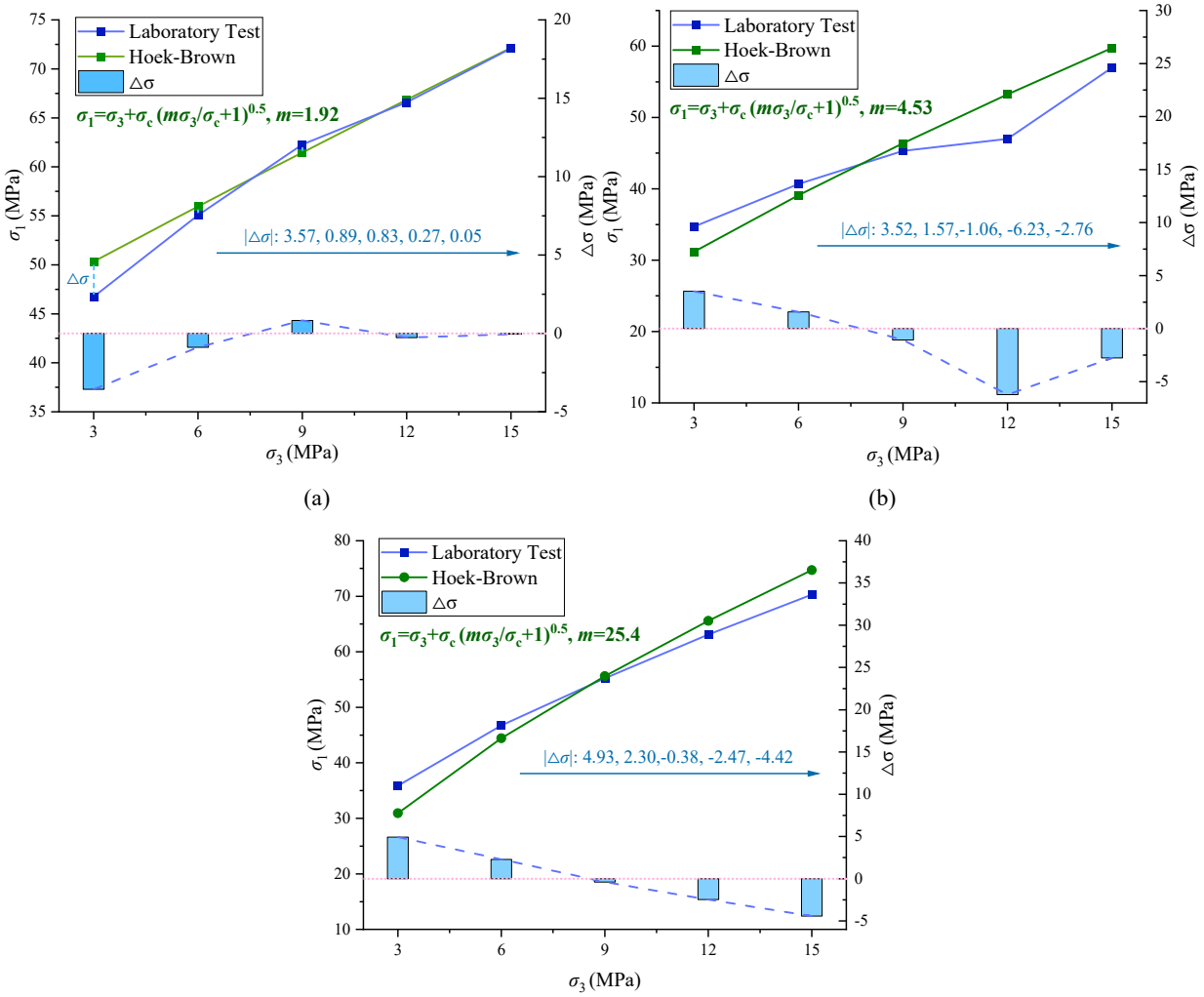


Figure 9. Curves of $\sigma_1 - \sigma_3$ under Hoek-Brown criterion. (a) Natural. (b) Water saturation. (c) Dehydration.

Figure 9 shows that the $\sigma_1 - \sigma_3$ curve under the Hoek–Brown criterion has a high correlation with the laboratory curve fitting, the maximum residual value does not exceed 7 MPa, and the floating proportion does not exceed 15%. This indicates that the Hoek–Brown criterion can well reflect the variation characteristics of the strength parameters of gypsum rocks under triaxial compression.

In the Hoek–Brown criterion, the formula for calculating tensile strength is

$$\sigma_t = \frac{2\sigma_c}{l + \sqrt{l^2 + 4}} \tag{9}$$

Substituting the l values calculated in Equation (8) and Figure 11 into Equation (9), the tensile strength and fitting parameters of the samples under the three conditions can be calculated as follows:

$$\begin{cases} \sigma_{t1} = 18.98MPa \\ \sigma_{t2} = 4.68MPa \\ \sigma_{t3} = 0.36MPa \end{cases}, \quad \begin{cases} l_1 = 1.92 \\ l_2 = 4.53 \\ l_3 = 25.4 \end{cases} \tag{10}$$

According to Equation (10), the tensile strength calculated by the Hoek–Brown criterion is also very different from the actual value, and the average value of the former is 4.3 times that of the latter. Based on the modified Mohr–Coulomb criterion, a modified Hoek–Brown criterion is also proposed, namely,

$$\sigma_t' = \alpha \frac{2\sigma_c}{l + \sqrt{l^2 + 4}} + \beta = \alpha\sigma_t + \beta \tag{11}$$

In Equation (11), α and β are the uniaxial strength correction coefficient and intercept correction coefficient, respectively. Through the approximation of the formula and data, the value of each parameter can be calculated as follows:

$$\begin{cases} \alpha = 0.19 \\ \beta = 0.18 \end{cases} \tag{12}$$

By substituting Equation (12) into Equation (11), the modified value $\sigma_t{}'$ of the tensile strength of each sample under different water content conditions is

$$\begin{cases} \sigma_{t1}{}' = 3.79MPa \\ \sigma_{t2}{}' = 1.07MPa \\ \sigma_{t3}{}' = 0.25MPa \end{cases} \tag{13}$$

According to Equation (13), compared with the original value, the average value calculated by the modified Hoek–Brown criterion is 8% different, is better than the modified Mohr–Coulomb criterion and can accurately reflect the variation in the strength parameters of samples in different states.

3.3.3 Balmer criterion

According to the Balmer criterion [48],

$$\sigma_1 = \sigma_c \left(1 + \frac{\sigma_3}{\sigma_t}\right)^b \tag{14}$$

where σ_c and σ_t are the uniaxial compressive strength and tensile strength of rock, respectively, and b is the test constant. According to Table 3, the test data are substituted into Equation (14), namely,

$$Balmer\ criterion: \begin{cases} 46.75 = \sigma_c \left(1 + \frac{3}{\sigma_t}\right)^b \\ 62.29 = \sigma_c \left(1 + \frac{9}{\sigma_t}\right)^b \\ 72.09 = \sigma_c \left(1 + \frac{15}{\sigma_t}\right)^b \end{cases}, \quad \begin{cases} 34.71 = \sigma_c \left(1 + \frac{3}{\sigma_t}\right)^b \\ 45.33 = \sigma_c \left(1 + \frac{9}{\sigma_t}\right)^b \\ 56.98 = \sigma_c \left(1 + \frac{15}{\sigma_t}\right)^b \end{cases}, \quad \begin{cases} 35.86 = \sigma_c \left(1 + \frac{3}{\sigma_t}\right)^b \\ 55.23 = \sigma_c \left(1 + \frac{9}{\sigma_t}\right)^b \\ 70.29 = \sigma_c \left(1 + \frac{15}{\sigma_t}\right)^b \end{cases} \tag{15}$$

According to Equation (15), σ_c and σ_t can be calculated by fitting:

$$\begin{cases} \sigma_{t1} = 3.88 \\ \sigma_{t2} = 1.45 \\ \sigma_{t3} = 0.22 \end{cases}, \quad \begin{cases} b_1 = 0.28 \\ b_2 = 0.37 \\ b_3 = 0.48 \end{cases} \tag{16}$$

According to Equation (16), the error of the average value calculated by the Balmer criterion compared with the original value is only 0.14%, which is the highest accuracy among the three criteria. This indicates that the Balmer criterion is most suitable to reflect the variation law of the strength parameters of samples in different states.

3.3.4 Comparison of the three criteria

Figure 10 shows compares the tensile strength values predicted by the three criteria. The upper right corner of Figure 10 shows the residual diagram of the calculated results of each criterion and the original value.

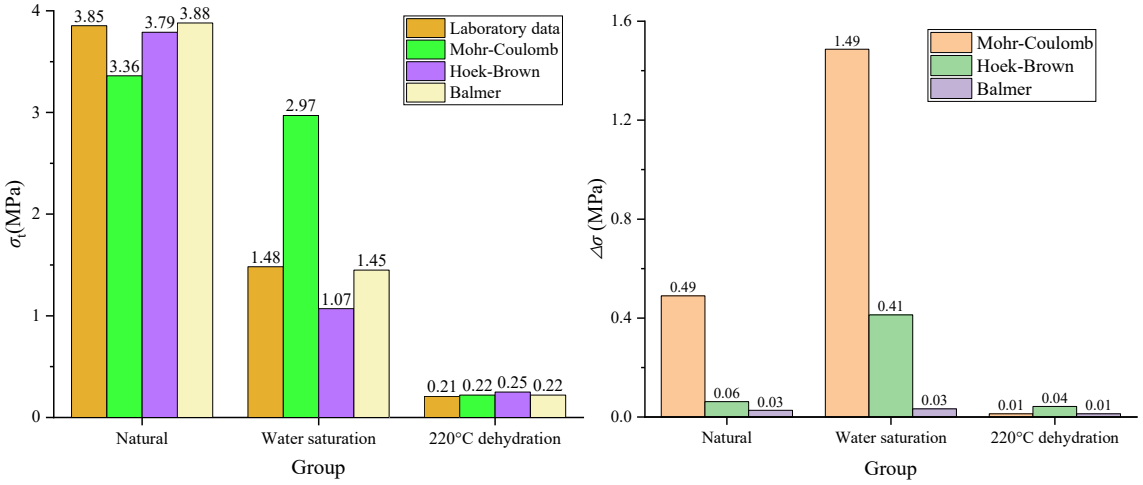


Figure 10. Comparison of predicted values of the three tensile strength criteria. (a) Predicted results. (b) $\triangle\sigma$.

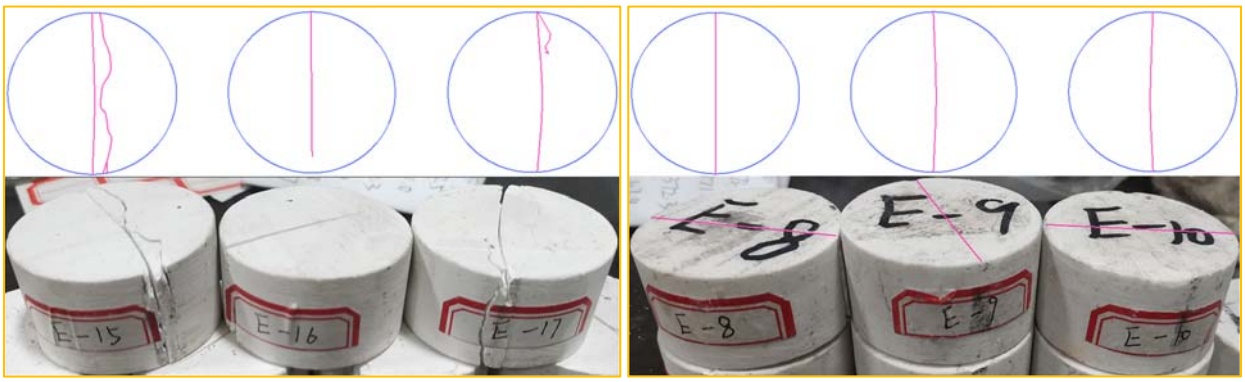
Figure 10 shows that the modified Mohr–Coulomb criterion is quite different from the actual value in evaluating the mechanical properties of the samples in the natural and saturated groups and is more accurate in evaluating the samples in the high-temperature dehydration group. This is because the Mohr–Coulomb criterion mainly considers the mechanical parameters in the conventional triaxial compression test, such as the internal friction angle and cohesion of the sample, and relies more on the triaxial test results of the sample. The more accurate the triaxial test results are, the closer the calculated tensile strength value is to the actual value.

Compared with the Mohr–Coulomb criterion, the modified Hoek–Brown criterion has significantly improved the fitting effect when evaluating the mechanical properties of the natural and saturated samples. This is because, in addition to the triaxial test results, the Hoek–Brown criterion also considers the uniaxial compressive strength of the samples, which makes the calculation results more accurate and the fitting accuracy higher than that with the Mohr–Coulomb criterion.

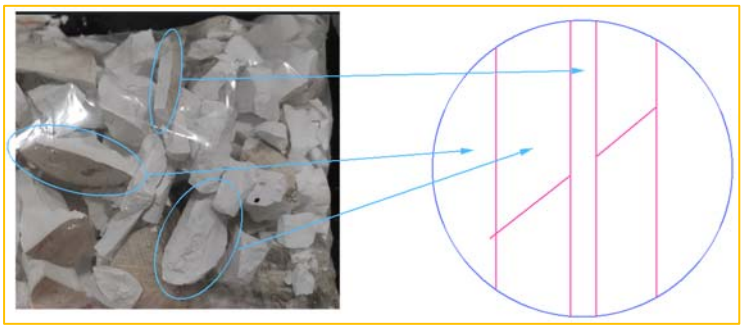
In addition to considering the results of a single triaxial test, the Balmer criterion also introduces exponential *b*, which changes the criterion equation from a polynomial to an exponential function, improves the adaptability of the equation and greatly improves its regression accuracy.

3.4 Failure characteristics

Rock failure is caused by fracture development, including microcrack initiation, propagation and macroscopic crack formation [49, 50]. To study the difference in the failure characteristics of samples with different moisture contents after the splitting test in Brazil, the plane crack distribution after failure was plotted, as shown in Figure 11.



(a) (b)



(c)

Figure 11. Failure characteristics of specimens after splitting test. (a) Natural. (b) Water saturation. (c) Dehydration.

Figure 11 shows that the specimens in the natural group exhibit obvious brittle failure characteristics, with cracks first appearing from the top of the disk and then gradually extending downwards. The samples in the natural group were not dehydrated or saturated, so their molecular structure was relatively stable, and the mutual attraction between adjacent parts was also strong. In the case of tensile failure of the disc, the middle adjacent part experiences secondary failure due to a large friction force, resulting in multiple cracks.

Compared with that of the natural group, the plasticity of the water-saturated group is enhanced, and the failure characteristics of the samples are not obvious. The specimen pieces after failure are relatively complete and can be pieced together into a disk again. This is because the higher water content reduces the brittleness of the sample, and more H_2O molecules surround $CaSO_4$ ions, playing a "buffer" role. When the specimen is damaged, the impact effect is greatly weakened, and secondary damage to the specimen is avoided.

Compared with the tensile strengths of the natural group and the water-saturated group, the tensile strength of the samples in the dehydration group decreased significantly, only approximately 0.2 MPa. In a splitting test, the specimen quickly reached its tensile strength and became fragmented. After roughly piecing the sample together, the crack direction of the sample is still vertical, and the sample is split into prisms, hemispheres, hexahedra with a parallelogram cross section and other shapes. This is because long-term dehydration causes the sample to lose most of its bound water and free water, the bonding force between $CaSO_4$ ions is greatly reduced, and the load that the sample can bear is also reduced. Therefore, it is easy to break under an external force.

4. Discussion

4.1 Plane stress distribution of the Brazilian disc

A schematic diagram of the traditional Brazilian splitting test is shown in Figure 12. In Figure 12, BC is the theoretical fracture surface of the sample, DE is the vertical segment of the theoretical fracture surface, r_1 is the distance from point A to point B, and r_2 is the distance from point A to C.

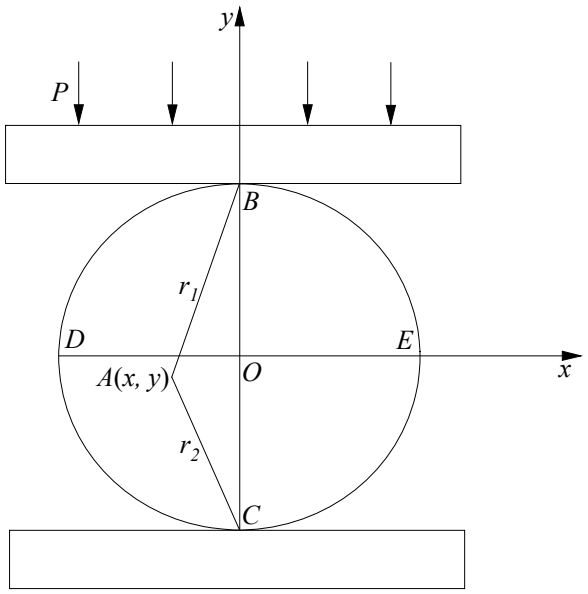


Figure 12. Schematic diagram of splitting test in Brazil.

Using the line of segment DE as the X-axis and the line of segment BC as the Y-axis, the XOY coordinate system is established, and the analytic formulas for stresses at A(x, y) are as follows [51]:

$$\begin{cases} \sigma_x = \dfrac{2P}{\pi t}\left\{\dfrac{x^2(R+y)}{[x^2+(R+y)^2]^2}+\dfrac{x^2(R-y)}{[x^2+(R-y)^2]^2}\right\}-\dfrac{P}{\pi Rt} \\ \sigma_y = \dfrac{2P}{\pi t}\left\{\dfrac{(R+y)^3}{[x^2+(R+y)^2]^2}+\dfrac{(R-y)^3}{[x^2+(R-y)^2]^2}\right\}-\dfrac{P}{\pi Rt} \\ \tau_{xy} = \dfrac{2P}{\pi t}\left\{\dfrac{x(R+y)^2}{[x^2+(R+y)^2]^2}+\dfrac{x(R-x)^2}{[x^2+(R-y)^2]^2}\right\} \end{cases} \tag{17}$$

where R is the radius, t is the thickness, P is the concentrated loading force, σ_x and σ_y are the normal stresses, and τ_{xy} is the shear stress.

Equation (17) reflects the plane stress distribution of the Brazilian splitting disk sample. When x=0, Equation (17) can be simplified as follows:

$$\begin{cases} \sigma_x = -\dfrac{P}{\pi Rt} \\ \sigma_y = \dfrac{2P}{\pi t}\left\{\dfrac{1}{R+y}+\dfrac{1}{R-y}\right\}-\dfrac{P}{\pi Rt} \\ \tau_{xy} = 0 \end{cases} \tag{18}$$

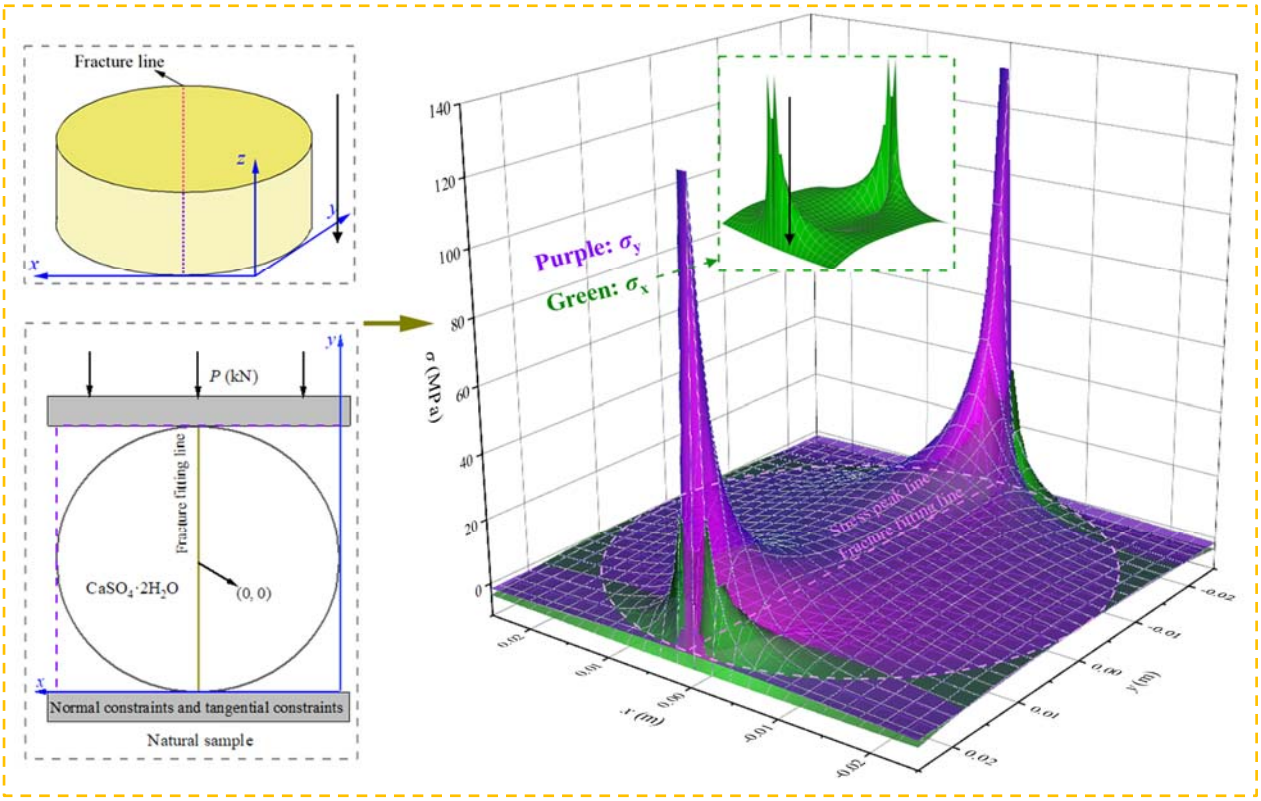
When y=0, Equation (17) can be written as

$$\begin{cases} \sigma_x = \dfrac{2P}{\pi t}\left\{\dfrac{x^2R}{(x^2+R^2)^2}+\dfrac{x^2R}{(x^2+R^2)^2}\right\}-\dfrac{P}{\pi Rt} \\ \sigma_y = \dfrac{2P}{\pi t}\left\{\dfrac{R^3}{(x^2+R^2)^2}+\dfrac{R^3}{(x^2+R^2)^2}\right\}-\dfrac{P}{\pi Rt} \\ \tau_{xy} = \dfrac{2P}{\pi t}\left\{\dfrac{xR^2}{[x^2+R^2]^2}+\dfrac{xR^2}{[x^2+R^2]^2}\right\} \end{cases} \tag{19}$$

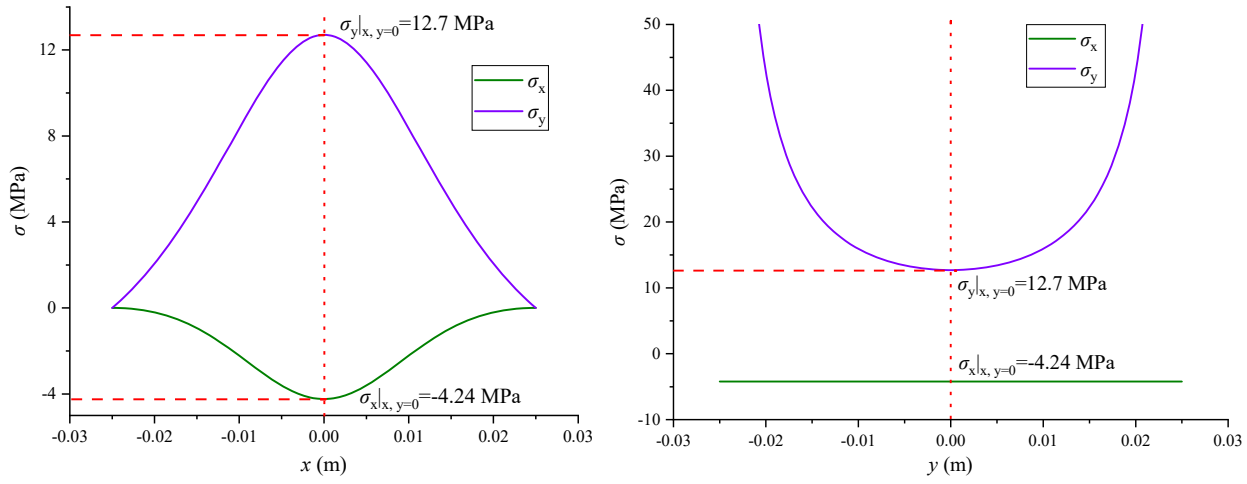
σ_x in Equation (18) is numerically equal to the tensile strength σ_t in Equation (1), which reflects the horizontal tensile stress at line segment BC (x=0). σ_y represents the vertical compressive stress at segment BC. $\tau_{xy} = 0$ means that at x=0, the shear stress is equal to zero. σ_x in Equation (19) reflects the horizontal tensile

stress value at line segment DE, which is y=0. σ_y reflects the vertical compressive stress at segment DE. $\tau_{xy} = 0$ means that at y=0, the shear stress is equal to zero.

To explore the plane stress distribution law of the Brazilian splitting disk sample, the plane distribution curves of horizontal and vertical stress in Equations (17) to (19) are drawn by taking the natural sample as an example, as shown in Figure 13. At the same time, to further analyse the variation trend of the horizontal and vertical stress of the sample at x=0 and y=0, the two stress–displacement curves in Figure 13 were fused to obtain Figure 14.



(a)



(b) (c)

Figure 13. Plane stress distribution of Brazilian split disk specimen. (a) Plane stress. (b) y=0. (c) x=0.

Figures 13 and 14 show that the vertical stress of the Brazilian disc sample presents the characteristics of a concentrated distribution. Along the X-axis direction, the vertical stress inside the sample increases first and then decreases with increasing x, and the vertical stress reaches its maximum at x=0. When x=0, along the Y-axis direction, the vertical stress in the sample first decreased and then increased with increasing y, and the vertical stress peaked at the line (0, ±0.025). From the above analysis, the vertical stress in the Brazilian disc sample is

compressive stress and concentrated at x=0, where the vertical load P directly acts. At x=0, the peak value of the vertical load appeared at both ends of the line, that is, the two ends of contact between the specimen and the indenter. From both ends of the specimen to the centre, the vertical stress gradually decreases because the gradient stress is generated under the action of external forces.

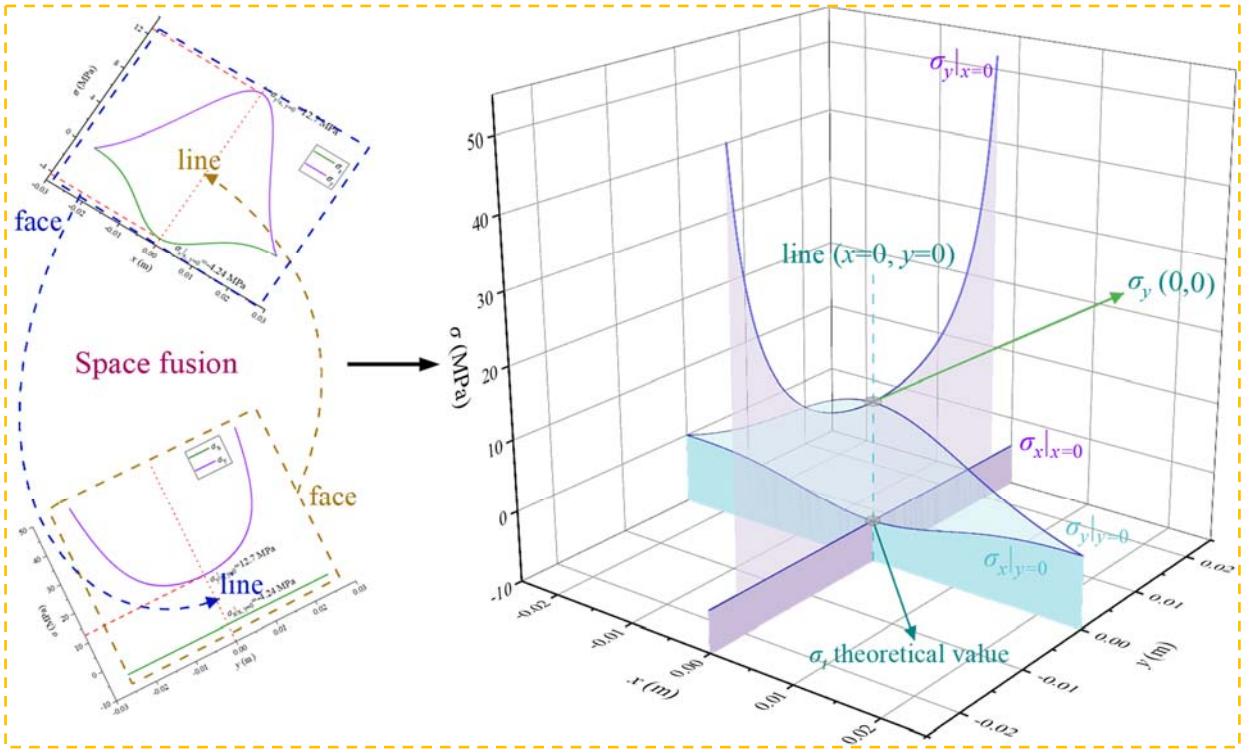


Figure 14. Stress-displacement curves of disk plane when x, y=0.

By observing the horizontal stress in Figures 13 and 14, the variation in the horizontal stress in the sample is relatively complex. At x=0, the horizontal stress of the sample is stable to 4.24 MPa, which is the theoretical tensile strength σ_t. For the convenience of plotting, the diameter and thickness of the sample are Φ = 0.05 m and d = 0.03 m, resulting in a difference between the conclusion and the laboratory results, which does not affect the analysis of the spatial distribution of stress in the sample. At y=0, along the X-axis direction, the horizontal stress inside the sample increases first and then decreases with the increase in x. From the above analysis, the horizontal stress in the Brazilian disc sample is tensile stress, which is concentrated at x=0 and uniformly distributed on the line directly affected by the vertical load P, and decreases from this line to both ends of the specimen, decreasing to 0 at the left and right ends of the specimen (±0.025, 0).

Figures 13 and 14 show an interesting phenomenon. The horizontal stress distribution in Figure 13 (the figure in the green dashed box) shows that there are only points (0, ±0.025) at both ends of the x=0 line that maintain the steady state of horizontal stress. When the two points are extended in any direction of X, the horizontal stress will be greatly increased. For example,

$$\begin{cases} \lim\limits_{x=0,y\to-0.025^{+}} \sigma_x = -4.24\ MPa \\ \lim\limits_{x=0,y\to-0.025^{-}} \sigma_x = 30\ MPa \\ \sigma_x(x=\pm0.002, \mathrm{y}=\pm0.025) = 40\ MPa \end{cases} \tag{20}$$

Equation (20) shows many strange phenomena; for example, the horizontal stress curve is not differentiable at (0,0.025) and oscillates abnormally at the end of the disk. Points (±0.002, ±0.025) are not in the range of the standard disk sample but in the boundary of the equivalent disk sample. To intuitively understand the causes of the horizontal stress peak, schematic drawings of the standard disc sample and equivalent disc sample are shown in Figure 15.

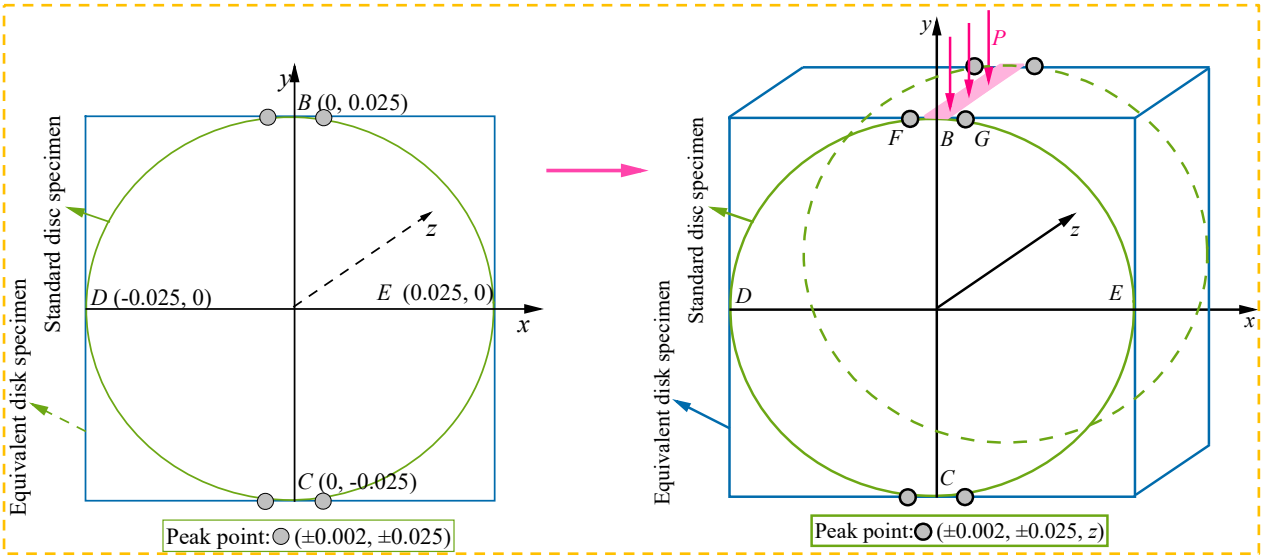


Figure 15. Standard disc sample and equivalent disc sample.

In Figure 15, the green circle is the section of the Brazilian disk sample, and the blue rectangle is the domain of stress represented by Equation (17). For the Brazilian splitting test, the part outside the green cylinder is not of practical significance, but the cause of its stress change is worth exploring.

As shown in Figure 15, the Z-axis is introduced to make the plane figure three-dimensional. Equation (17) expresses the cube with local forces on the top. When the cube does not exist, there is no constraint around the disk sample; in arc $\widehat{DF}$ and $\widehat{EG}$ sections prone to deformation, it is not easy to produce a stress concentration. However, when the cube exists, it is equivalent to adding constraints around the disk, leading to the horizontal stress peak at (±0.002, ±0.025) due to stress concentration. This is the reason why the left and right limits of the horizontal stress curve in Equation (20) are not equal at point (0, ±0.025) and the stress is concentrated at point (±0.002, ±0.025).

4.2 Plane strain distribution of the Brazilian disc

In Section 3.3 and Section 4.1, we analysed the strength characteristics and stress distribution characteristics of the sample in the splitting test, but the analysis is from the perspective of stress. To further explore the deformation mechanism of the sample in the Brazilian splitting test, 3DEC software was used to simulate the Brazilian splitting test by taking the natural sample as an example.

The established model was divided into three parts, namely, 1 sample and 2 indenters, as shown in Figure 16.

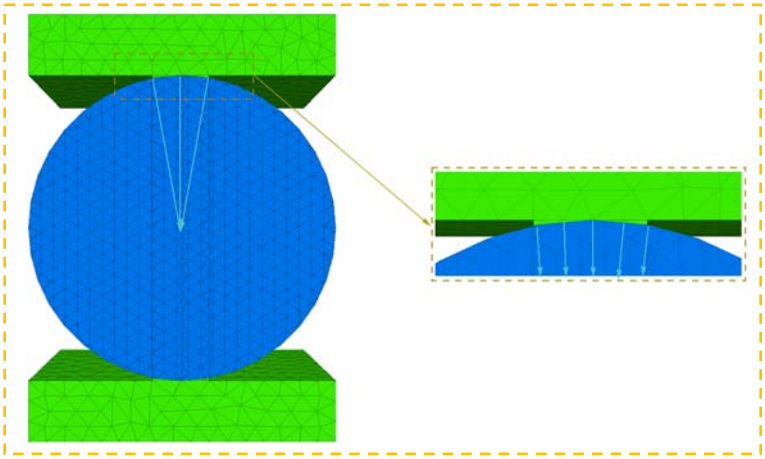


Figure 16. 3DEC model.

In Figure 16, the indenter is rectangular in shape, and the size is 50 mm × 25 mm × 10 mm. The sample size is Φ 50 mm × d 25 mm, which is consistent with the theoretical sample size in Section 4.1. The contact end between the indenter and the specimen is arc-shaped to ensure that the specimen can be tightly attached.

The constitutive parameters of the model are as follows: the indenter is set as linear elastic constitutive, the default is isotropic, and sliding and tensile failure are not allowed. The sample is set as the Mohr–Coulomb constitutive. According to the data in Table 3 and the previous test results, the strength parameter values are set, as shown in Table 4 (34).

Table 4. Mechanical parameters of coal seam roof and floor

Group	c (MPa)	φ (°)	E (GPa)	E_{50} (GPa)
Natural	13.18	27	3.87	2.95
Water saturation	11.39	15	2.09	1.36
Dehydration	8.50	28.7	1.15	0.58

The boundary conditions of the model are as follows: the three-way velocity of the fixed lower indenter is 0 to fix the model; the tangential velocity of the upper indenter is fixed to 0 to prevent the upper indenter from generating displacement outside the normal direction during loading and then generating shear stress on the surface of the sample (SZX, SZY, etc.). After the boundary conditions are applied, the prestressing force is set to 0.1 MPa, namely,

In situ stress <*sxx, syy, szz, sxy, sxz, syz*> = <0, 0, 0.1e6, 0, 0, 0>

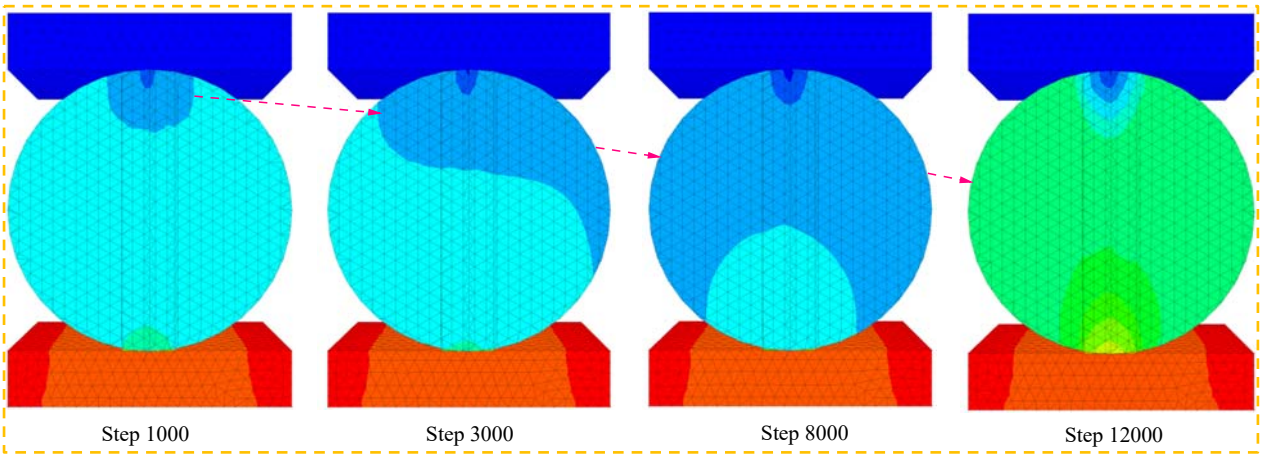
Since the force on the block under the action of the testing machine is not completely uniform, a stress gradient is added from the centre of the block to each surface (in the model, the centre of the sample is the origin), namely,

*z*grad <*sxxz, syyz, szzz, sxyz, sxzz, syzz*> = <5, 5, 5, 0, 0, 0>

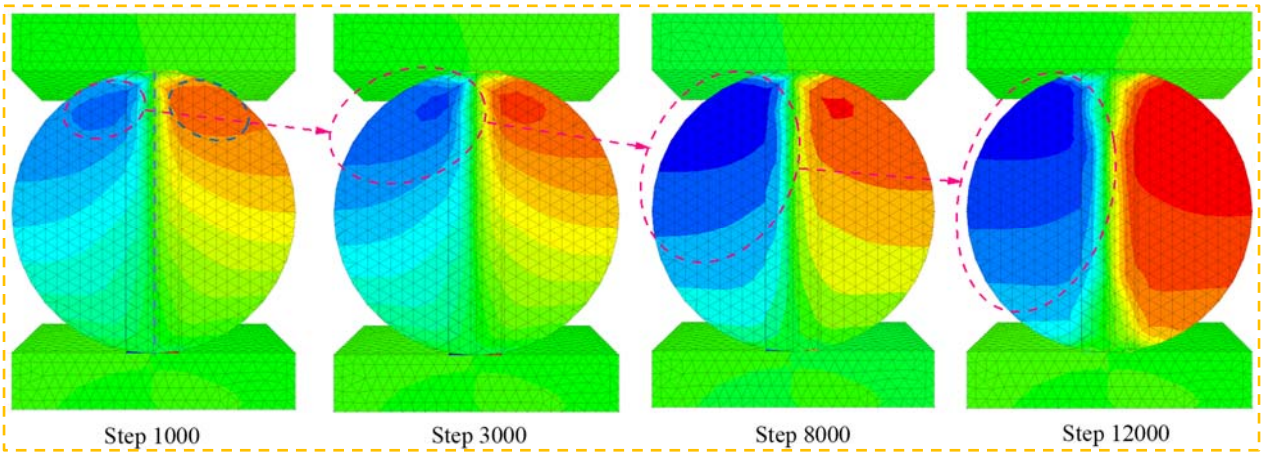
According to the above steps, the stress distribution applied to the media is shown in Equation (21), where σ_{xx}^{0} is the stress at the origin of coordinates.

$$\sigma_{zz} = \sigma_{zz}^{0} + (szzx) * x + (szzy) * y + (szzz) * z \tag{21}$$

After the initial stress is applied, the displacement test is carried out on the sample, and the upper indenter is loaded with the displacement control method at a speed of -0.003 mm/s. In the loading process, the displacement cloud diagram of the sample is shown in Figure 17.



(a)



(b)

Figure 17. Cloud diagram of displacement distribution.(a) Vertical displacement.(b) Horizontal displacement.

Figure 17(a) shows that during the loading process, the deformation of the sample in the vertical direction first arises from the top tip and spreads downwards in a "ripple" shape with the prolongation of the loading time. This is consistent with the conventional compression test, and the deformation propagates from near the indenter to far away from the indenter. As seen from Figure 14, at x=0 and y=0, the vertical stress of the sample is 3 times the horizontal stress, while the compressive strength of the general rock material is more than 8 times the tensile strength, which eventually leads to tensile failure of the sample.

Figure 17(b) shows that during the loading process, the deformation of the sample in the horizontal direction first arises from both sides of the upper tip and spreads downwards with the extension of the loading time. Taking the red dotted circle in Figure 17 as an example, the colour depth represents the size of the deformation. The darker the colour is, the greater the deformation. At the beginning of loading, the expansion deformation appeared on both sides of the upper part of the sample along the centreline, concentrated in the oval area on both sides, and then extended to both ends and the lower side until it propagated to the bottom. While the original deformation propagates downwards, the new deformation also gradually arises and continues to spread, resulting in gradient displacement. According to the above analysis, in the process of the splitting test in Brazil, the strain in the upper part is always greater than that in the lower part. Under the continuous loading of the indenter, the upper part of the sample reaches its tensile strength first, resulting in failure.

This does not conflict with the horizontal stress distribution laws described in Figure 13 and Equation (17). Equation (17) illustrates the distribution law of disc stress in the steady state, while Figure 17 (b) shows the variation in displacement inside the specimen during loading. During the loading process, the horizontal deformation of the upper part of the sample was always greater than that of the lower part because the sample did not reach a stable state. After the loading is stopped and equilibrium is calculated, the horizontal displacement in the sample along both sides of the centreline shows a stable distribution.

5. Conclusion

By laboratory tests, theoretical analysis and numerical simulation, the physical and mechanical properties of specimens under different moisture content conditions were investigated in this paper. On this basis, the plane stress and strain distributions of Brazilian split specimens were analysed in depth. The conclusions are as follows.

1) The longitudinal wave velocity, microscopic characteristics and composition of the samples are closely related to the water content. The larger the water content of the sample is, the higher the content of $CaSO_4 \cdot 2H_2O$, the more flocculent structures on its surface, and the higher the longitudinal wave propagation speed. The natural sample contains more $CaSO_4 \cdot 0.5H_2O$, and its tensile strength is the highest. The content of $CaSO_4 \cdot 2H_2O$ in the saturated samples increases, which leads to a decrease in tensile strength. The dehydrated samples lose most of their free water and structural water, resulting in the most obvious deterioration in their properties.

2) The modified Hoek–Brown criterion considers the influence of the uniaxial compressive strength of the sample, and the fitting effect is obviously improved compared to that of the modified Mohr–Coulomb criterion. Thus, the Balmer criterion introduces exponential parameter b, which changes the criterion equation from a polynomial to an exponential function, greatly improves its regression accuracy.

3) The samples of the natural group are prone to secondary failure in tensile testing, resulting in multiple cracks. In the saturated group samples, H_2O molecules dissociate around $CaSO_4$ ions, which plays a role in "buffering", and secondary damage is avoided. The samples in the dehydration group lose most of their bound water and free water, and the binding force between $CaSO_4$ ions is greatly reduced. Thus, fracture occurs easily under the action of an external force.

4) The vertical stress of the Brazilian disk sample is compressive stress, which mainly shows concentrated distribution characteristics. The horizontal stress is mainly tensile stress, and the value at x=0 is the theoretical tensile strength. The horizontal stress is uniformly distributed on the line directly affected by vertical load P, decreases from this line segment to both ends of the specimen, and reduces to 0 at the left and right ends of the specimen.

5) The horizontal deformation of the sample first originates from both sides of the disk tip and spreads downwards in an arc with the extension of the loading time. The horizontal strain in the upper part of the disk is always greater than that in the lower part. Under the continuous loading of the indenter, the upper part of the sample reaches its tensile strength first, resulting in failure.

6. Variable annotations

Variate	Annotation	Variate	Annotation
m	Quality (g)	σ_x	Horizontal stress (MPa)
f_w	Water content	σ_y	Vertical stress (MPa)
ρ	Density (g/cm^3)	τ_{xy}	Shear stress (MPa)
v	Longitudinal wave velocity (m/s)	σ_1	The maximum principal stresses (MPa)
σ_t	Tensile Strength (MPa)	σ_3	The minimum principal stresses (MPa)
c	Cohesion (MPa)	σ_c	Uniaxial compressive strength (MPa)
φ	Internal friction angle (°)	σ	Normal stress (MPa)
E	Elasticity modulus (GPa)	l	Empirical parameter
E_{50}	Modulus of deformation (GPa)	b	Test constant.

7. Statements

7.1 Funding

Supported by Scientific Research Foundation of State Key Lab of Coal Mine Disaster Dynamics and Control (Project Approval Number: 2011DA105287-zd201804) and National Natural Science Foundation of China (No. 51974104).

7.2 Competing Interests

The authors have no relevant financial or non-financial interests to disclose.

7.3 Author Contributions

Wang Chongyang: Data curation, Writing- Original draft preparation. **Zhang Dongming:** Writing-Reviewing and Editing. **Wei Sijiang:** Funding acquisition, Investigation. **Yang Yushun:** Supervision, Validation. **Yu Beichen:** Conceptualization, Methodology. **Pan Yisha:** Methodology.

7.4 Data Availability

The datasets generated during and analyzed during the current study are available from the corresponding author on reasonable request.

References

[1] Y. Gan, S. Wu, Y. Ren, G. Zhang, Evaluation indexes of granite splitting failure based on RA and AF of AE parameters. *Rock and Soil Mechanics*, 41(7) (2020): 2324-2332. https://doi.org/10.16285/j.rsm.2019.1460.

[2] H. Deng, J. Li, M. Zhu, R. Wang, X. Yuan, S. Luo, Research on effect of disc thickness-to-diameter ratio on splitting tensile strength of rock. *Chinese Journal of Rock Mechanics and Engineering*, 31(4) (2012): 792.

[3] Y. Han, Z. Wang, Y. Tang, Mechanical behavior of different rocks in the splitting test. *Journal of China University of Mining and Technology*, 49(5) (2020):863. https://doi.org/10.13247/j.cnki.jcumt. 001192.

[4] W. Yao, K. Xia, X. Li, Non-local failure theory and two-parameter tensile strength model for semi-circular bending tests of granitic rocks. *International Journal of Rock Mechanics and Mining Sciences*. 110 (2018),9-18. https://doi.org/10.1016/j.ijrmms.2018.07.0020

[5] F. Nascimento, A. Guimaraes, C. Castro, Comparative study on permanent deformation in asphalt mixtures from indirect tensile strength testing and laboratory wheel tracking. *Construction and Building Materials*. 305 (2021). https://doi.org/10.1016/j.conbuildmat.2021.124736.

[6] N. Wu, J. Fu, Z. Zhu, B. Sun, 2020. Experimental study on the dynamic behavior of the Brazilian disc sample of rock material. *International Journal of Rock Mechanics and Mining Sciences*. 130 (2020). https://doi.org/10.1016/ j.ijrmms.2020.104326.

[7] T. Saksala, M. Hokka, V. Kuokkala, J. Makinen, 2013. Numerical modeling and experimentation of dynamic Brazilian disc test on Kuru granite. *International Journal of Rock Mechanics and Mining Sciences*. 59 (2013),128-138. https:// doi.org/10.1016/j.ijrmms.2012.12.018.

[8] D. Shen, X. Shi, S. Zhu, X. Duan, J. Zhang, Relationship between tensile Young's modulus and strength of fly ash high strength concrete at early age. *Construction and Building Materials*. 123 (2016), 317-326. https:// doi.org/10.1016/j.conbuildmat.2016.06.145.

[9] Y. Li, J. Li, Relationship between fracture area and tensile strength of cement paste with supplementary cementitious materials. *Construction and Building Materials*. 79 (2015), 223-228. https://doi.org/10.1016/j.conbuildmat.2015.01.052.

[10] R. Verma, G. Nguyen, M. Karakus, A. Taheri, Capturing snapback in indirect tensile testing using AUSBIT-Adelaide University Snap-Back Indirect Tensile test. *International Journal of Rock Mechanics and Mining Sciences*. (2021). https:// doi.org/10.1016/j.ijrmms.2021.104897.

[11] P. Lochan, M. Polak, Determination of tensile strength of GFRP bars using flexure tests. *Construction and Building Materials*. 314 (2021). https://doi.org/10.1016/j.conbuildmat.2021.125630.

[12] C. Gaedicke, A. Torres, K. Huynh, A. Marines, A method to correlate splitting tensile strength and compressive strength of pervious concrete cylinders and cores. *Construction and Building Materials*. 125 (2016), 271-278 https://doi.org/10.1016/j.conbuildmat.2016.08.031.

[13] A. Mardoukhi, Y. Mardoukhi, M. Hokka, V. Kuokkala, Effects of heat shock on the dynamic tensile behavior of granitic rocks. *Rock Mechanics and Rock Engineering*. 50(5) (2017),1171-1182. https://doi.org/10.1007/s00603-017-1168-4.

[14] A. Mardoukhi, Y. Mardoukhi, M. Hokka, V. Kuokkala, Effects of test temperature and low temperature thermal cycling on the dynamic tensile strength of granitic rocks. *Rock Mechanics and Rock Engineering*. 54(1) (2021),443-454. https://doi.org/10.1007/s00603-020-02253-6.

[15] S. Zhao, X. Ding, M. Zhao, C. Li, S. Pei, Experimental study on tensile strength development of concrete with manufactured sand. *Construction and Building Materials*. 138 (2017), 247-253. https://doi.org/10.1016/j.conbuildmat.2017.01.093.

[16] Y. Ren, V. Vavrycuk, S. Wu, Y. Gao, Accurate moment tensor inversion of acoustic emissions and its application to Brazilian splitting test. *International Journal of Rock Mechanics and Mining Sciences*. 141 (2021), https://doi.org/ 10.1016/j.ijrmms.2021.104707.

[17] P. Hou, Y. Xue, F. Gao, F. Dou, S. Su, C. Cai, C. Zhu, Effect of liquid nitrogen cooling on mechanical characteristics and fracture morphology of layer coal under Brazilian splitting test. *International Journal of Rock Mechanics and Mining Sciences*. 151 (2022). https://doi.org/10.1016/j.ijrmms.2021.105026.

[18] Y. Ma, H. Huang, DEM analysis of failure mechanisms in the intact Brazilian test. *International Journal of Rock Mechanics and Mining Sciences* (2018). https://doi.org/102,109-119. 10.1016/j.ijrmms.2017.11.010.

[19] N. Erarslan, D. Williams, Experimental, numerical and analytical studies on tensile strength of rocks. *International Journal of Rock Mechanics and Mining Sciences*. 49 (2012), 21-30. https:// doi.org/ 10.1016/j.ijrmms. 2011.11.007.

[20] N. Erarslan, Z. Liang, D. Williams, Experimental and numerical studies on determination of indirect tensile strength of rocks. *Rock Mechanics and Rock Engineering*. 45 (2012), 739–751. https://doi.org/10. 1007/s00603-011-0205-y.

[21] O. Mahabadi, B. Cottrell, G. Grasselli, An example of realistic modelling of rock dynamics problems: fem/dem simulation of dynamic brazilian test on barre granite. *Rock Mechanics and Rock Engineering*. 43(6) (2010), 707-716. https://doi.org/10.1007/s00603-010-0092-7.

[22] Z. Liang, C. Tang, Y. Zhang, T. Ma, On probability model of physico-mechanical parameters of quasi-brittle materials and associated mechanical failure behaviors. *Chinese Journal of Rock Mechanics and Engineering*, 27(4) (2008): 718-727. https://doi.org/10.3321/j.issn:1000-6915.2008.04.010.

[23] Z. Yang, B. He, L. Xie, C. Li, J. Wang, Strength and failure modes of shale based on Brazilian test. *Rock and Soil Mechanics*, 36(12) (2015): 3447. https://doi.org/10.16285/j.rsm.2015.12.015.

[24] D. Aggelis, Classification of cracking mode in concrete by acoustic emission parameters. *Mechanics Research Communications*, 38(3) (2011):153-157. https://doi.org/0.1016/j.mechrescom.2011.03.007.

[25] Q. Jiang, J. Cui, X. Feng, G. Liu, B. Wang, T. Liu, Y. Lv, Stochastic statistics and probability distribution estimation of mechanical parameters of basalt. *Rock and Soil Mechanics*, 38(3) (2017): 784. https:// doi.org/10.16285/j.rsm.2017.03.022.

[26] M. Du, P. Pan, W. Ji, Z. Zhang, Y. Gao, Time-space laws of failure process of carbonaceous shale in Brazilian split test. *Rock and Soil Mechanics*, 37(12) (2016): 3437-3446. https://doi.org/10.16285/j.rsm.2016.12.012.

[27] X. Li, L. Luo, C. Li, Experimental study of directivity effect of rock interface under Brazilian splitting. *Chinese Journal of Engineering*, 39(9) (2017):1295-1304. https://doi.org/10.13374/j.issn2095-9389. 2017. 09.001.

[28] S. Yang, Y. Li, Y. Huang, W. Tian, Particle flow analysis of macroscopic and microscopic mechanical properties of Brazilian disc containing a hole under splitting test. *Journal of China University of Mining and Technology*, 48(5) (2019): 984-992. https://doi.org/10.13247/j.cnki.jcumt.001055.

[29] D. Zhang, R. Gamage, M. Perera, C. Zhang, W. Wanniarachchi, (2017). Influence of water saturation on the mechanical behaviour of low-permeability reservoir rocks. *Energies*. 10(2), 236; https://doi.org/10.3390/ en10020236.

[30] Z. You, Y. Ma, Z. Wang, J. Ma, Tensile strength variation of a silty clay under different temperature and moisture conditions. *Cold Regions Science and Technology*. 189. https://doi.org/10.1016/j.coldregions.2021. 103314.

[31] T. Kim, C. Hwang, Modeling of tensile strength on moist granular earth material at low water content. *Engineering Geology.* 69(3-4),233-244. https://doi.org/10.1016/S0013-7952(02)00284-3.

[32] H. Li, C. Tang, Q. Cheng, S. Li, X. Gong, B. Shi, (2019). Tensile strength of clayey soil and the strain analysis based on image processing techniques. *Engineering Geology*. 253, 137-148. https://doi.org/10.1016/j.enggeo.2019.03.017.

[33] B. Vasarhelyi, (2003). Some observations regarding the strength and deformability of sandstones in dry and saturated conditions. *Bulletin of Engineering Geology and the Environment*. 62, 245–249. https://doi.org/10. 1007/s10064-002-0186-x.

[34] Z. Zhou, X. Cai, W. Cao, X. Li, C. Xiong, (2016). Influence of Water Content on Mechanical Properties of Rock in Both Saturation and Drying Processes. *Rock Mechanics and Rock Engineering*. 49, 3009–3025. https://doi.org/10.1007/s00603-016-0987-z.

[35] Z. Erguler, R. Ulusay. Water-induced variations in mechanical properties of clay-bearing rocks. *International Journal of Rock Mechanics and Mining Sciences*.46(2), 355-370. https://doi. org/10.1016/j.ijrmms.2008. 07.002.

[36] A. Daraei, S. Zare, (2018). Effect of Water Content Variations on Critical and Failure Strains of Rock. *KSCE Journal of Civil Engineering*. 22, 3331–3339. https://doi.org/10.1007/s12205-018-0592-7.

[37] C. Tang, X. Pei, D. Wang, B. Shi, J. Li, (2015). Tensile Strength of Compacted Clayey Soil. *Journal of Geotechnical and Geoenvironmental Engineering*. 141(4). https://doi.org/10.1061/(asce)gt. 1943-5606. 0001267.

[38] S. Wei, C. Wang, Y. Yang, M. Wang, Physical and mechanical properties of gypsum-like rock materials. *Advances in Civil Engineering*, (2020), 1–17, https://doi.org/10.1155/2020/3703706.

[39] C. Wang, Study on Low-Frequency Dynamic Physico-Mechanical Properties of Gypsum Rocks. MSc Thesis, *Henan Polytechnic University*. (2021).

[40] C. Wang, S. Wei, Y. Pan, S. Zhang, Experimental study on fatigue life of gypsum-like rock under uniaxial compression with different loading frequencies. *Pure and Applied Geophysics*, 179 (2022), https://doi.org/ 10.1007/ s00024-022-02966-5.

[41] C. Wang, S. Wei, M. Wang, C. Xu, S. Zhang, Rockburst characteristics of gypsum-like rocks after fatigue cyclic loading. *Arabian Journal of Geosciences*, 15(15) (2022). https://doi.org/10.1007/s12517-022-10636-y.

[42] Y. Pan, C. Wang, Y. Wang, Mechanical degradation mechanism of rock under seismic disturbance stress. *Quarterly Journal of Engineering Geology and Hydrogeology*, 55 (2022). https://doi.org/10.1144/qjegh 2022 -007.

[43] S. Chen, Z. Du, Z. Zhang, H. Zhang, Z. Xia, F. Feng, (2020), Effects of chloride on the early mechanical properties and microstructure of gangue-cemented paste backfill, *Construction and Building Materials*, 235(2): 117504. https://doi.org/10.1016/j.conbuildmat.2019.117504.

[44] M. Dolezelova, L. Scheinherrova, J. Krejsova, A. Vimmrova, Effect of high temperatures on gypsum-based composites. *Construction and Building Materials.* 168 (2018) 82-90. https://doi.org/10.1016/j.conbuildmat. 2018.02.101.

[45] X. Shi, Y. Meng, G. Li, Comparative analyses of several rock strength criteria. *Rock and Soil Mechanics*, 32(1) (2011): 209-215. https:// doi.org/10.16285/j.rsm.2011.s1.022.

[46] E. Hoek, E. Brown, Empirical strength criterion for rock masses. *Journal of Geotechnical and Geoenvironmental Engineering*, 106 (GT9) (1980), 1013-1035. https://doi.org/10.1016/0022-1694(80) 90029-3.

[47] E. Hoek, Strength of rock and rock masses. *International Society of Rock Mechanics News Journal*, 2(2) (1994): 4-16.

[48] L. Wu, Study on rock mass strength criterion. MSc Thesis, *Chang 'an University*. (2004).

[49] S. Chen, Z. Xia, F. Feng, D. Yin, (2021). Numerical study on strength and failure characteristics of rock samples with different hole defects. *Bulletin of Engineering Geology and the Environment*. 80(2): 1523-1540. https://doi.org/10.1007/s10064-020-01964-y

[50] J. Jiang, X. Feng, C. Yang, G. Su, Failure characteristics of surrounding rocks along the radial direction of underground excavations: An experimental study. *Engineering Geology*. 281 (2021). https://doi.org/10. 1016/j.enggeo.2020.105984.

[51] N. Muskhelishvili, Some basic problems of mathematical theory of elasticity. *Axel Springer.* (1977).